The Path to Actinorhodin: Regio- and Stereoselective Ketone Reduction by a Type II Polyketide Ketoreductase Revealed in Atomistic Detail

Stefano A. Serapian,[†,^] John Crosby,[‡] Matthew P. Crump[‡] and Marc W. van der Kamp,[*,†]

[†]School of Biochemistry, University of Bristol, University Walk, Bristol, BS8 1TD, United Kingdom

[‡]School of Chemistry, University of Bristol, Cantock's Close, Bristol, BS8 1TS, United Kingdom

KEYWORDS: Polyketide synthesis, Protein-protein Docking, Computational Enzymology, 2D-NMR, QM/MM

ABSTRACT: In type II polyketide synthases (PKSs), which typically biosynthesize several antibiotic and antitumor compounds, the substrate is a growing polyketide chain, shuttled between individual PKS enzymes whilst covalently tethered to an acyl carrier protein (ACP): this requires the ACP interacting with a series of different enzymes in succession. During biosynthesis of the antibiotic actinorhodin, produced by *Streptomyces cœlicolor*, one such key binding event is between an ACP carrying a 16-carbon octaketide chain (*act*ACP) and a ketoreductase (*act*KR). Once the octaketide is bound inside *act*KR, it is likely cyclized between C7 and C12 and regioselective reduction of the ketone at C9 occurs: how these elegant chemical and conformational changes are controlled is not yet known. Here, we perform protein-protein docking, protein NMR, and extensive molecular dynamics simulations to reveal a probable mode of association between *act*ACP and *act*KR; we obtain and analyze a detailed model of the C7-C12-cyclized octaketide within the *act*KR active site; and confirm this model through multiscale (QM/MM) reaction simulations of the key ketoreduction step. Molecular dynamics simulations show that the most thermodynamically stable cyclized octaketide isomer *(7S,12R)* also gives rise to the most 'reactive conformations' for ketoreduction. Subsequent reaction simulations show that ketoreduction is stereoselective as well as regioselective, resulting in an *S*-alcohol. Our simulations further indicate several conserved residues that may be involved in selectivity of C7-12 cyclisation and C9 ketoreduction. The detailed insights obtained on ACP-based substrate presentation in type II PKSs will help with the design of nonendogenous ACP-ketoreductase systems capable of biosynthesizing non-natural polyketides.

Introduction

In type II polyketide synthases (PKS)[1] a series of standalone enzymes grow a finite-sized polyketide chain and typically convert it into a complex natural product. An acyl carrier protein (ACP) in conjunction with a chain-length factor (CLF) and ketosynthase (KS) heterodimer catalyze the basic carbon backbone assembly and define a minimal PKS complex.[1-2] The polyketide alternates between being thioester linked to the KS or the phosphopantetheinyl (PPant) prosthetic group of the ACP (Chart 1) during each round of Claisen condensation of malonyl ACP and the KS bound polyketide. The ACP also shuttles the elongated substrate between subsequent tailoring PKS components that begin the defined series of chemical transformations that include reduction, cyclisation, aromatization, dimerization and numerous other functionalizations.[2-3] The archetypal type II PKS of the actinomycete bacterium *Streptomyces cœlicolor* (*act*PKS)[2-4] biosynthesizes the antibiotic actinorhodin (Chart 1) from a linear 16-carbon octaketide chain (**1**). After chain elongation, the actinorhodin ketoreductase (*act*KR) likely specifically cyclizes the polyketide between C7 and C12 (**2**) and reduces the ketone at C9 (**3**) while it remains attached to the actinorhodin ACP (*act*ACP) (Scheme 1). Extensive work by Tsai and co-workers has found the KR to be capable of remarkable regio- and stereocontrol[5-8] and this class of enzymes has attracted interest for their use as biocatalysts in the stereoselective synthesis of small chiral alcohols from achiral ketones.[9-14] KRs can be mutated to alter and tune their biocatalytic properties as standalone enzymes or used in 'combinatorial biosynthesis' alongside other enzyme components from a PKS to produce polyketide derivatives with novel functionality.[15-17]

Chart 1. *Act*PKS octaketide and its products.[a]

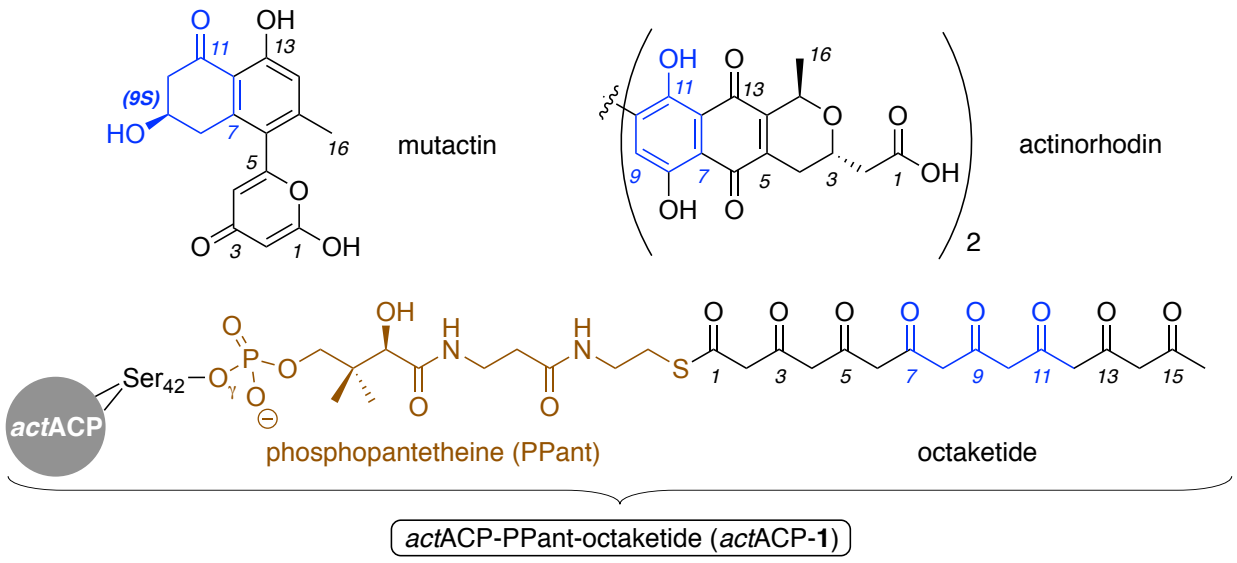

[a]*Atoms in blue denote the portion of PPant-octaketide (**1**) that forms the six-membered ring upon cyclization*

.

Scheme 1. Formation of cyclized octaketide 2 (A) and subsequent reactions (B).[a]

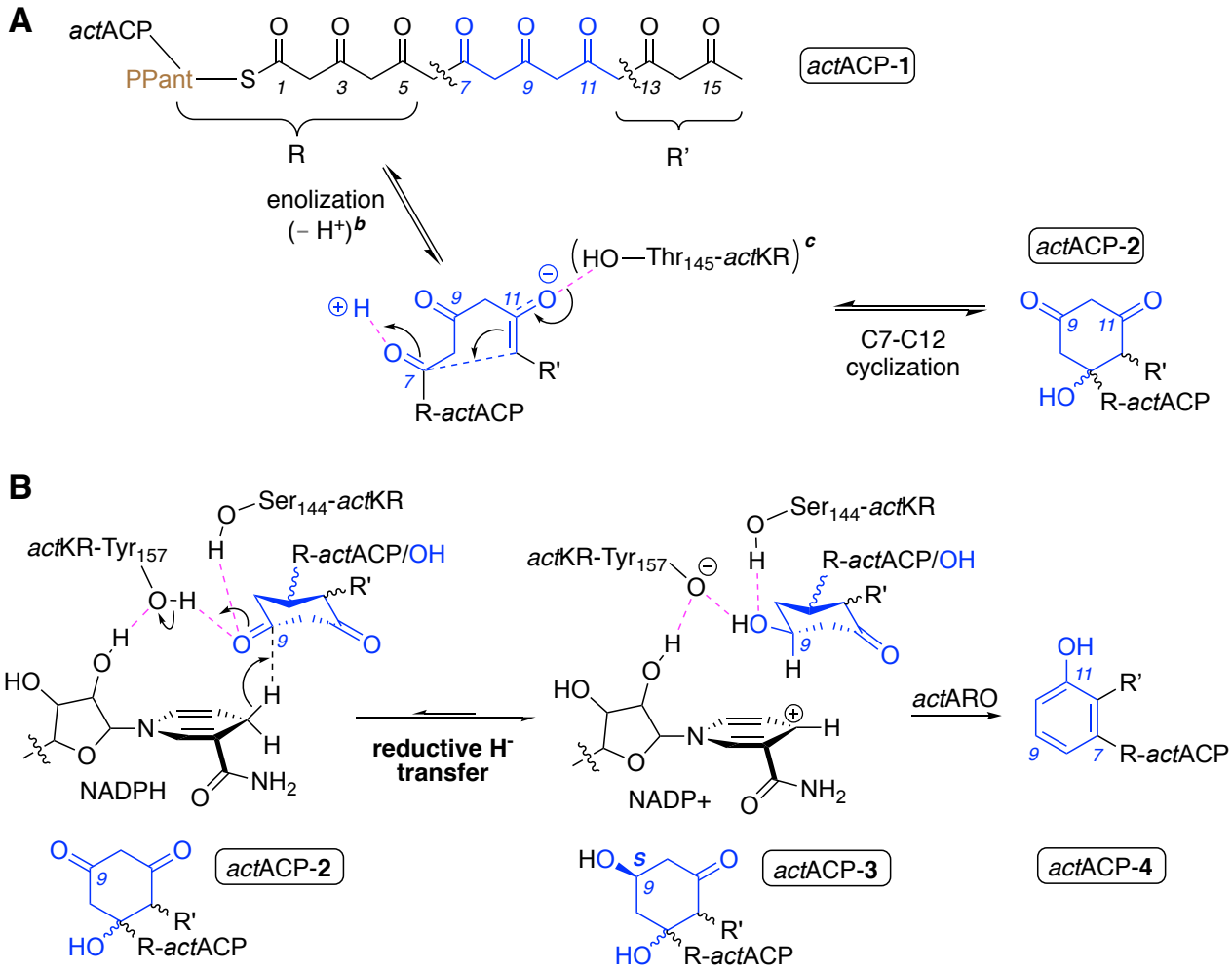

[a]Atoms in blue denote the portion of PPant-octaketide (**1**) forming the six-membered ring in the cyclized intermediate (**2**). Dotted magenta lines denote hydrogen bonds. [b] Loss of a proton on C12. [c] The exact role of *act*KR:Thr145 in cyclization is not established.

Experimental and theoretical studies have confirmed that the PPant group,[18] the α2 helix,[19] and the α3 helix (acting as a conformational 'gatekeeper'; Figure 1b)[20] are all crucial in recognition of PKS and fatty acid synthase (FAS) ACPs[21] by their enzymatic partners.[22] In the actinorhodin system, the labile post-assembly octaketide substrate may be partially protected by *act*ACP[23] whilst being transported to the *act*KR.[1] The *act*ACP shuttle binds to one monomer of the homotetrameric *act*KR, whereupon **1** is unsheathed[1] into its active site, which is characteristically narrow and restrictive.[5] In the specific case of the *act*KR – *act*ACP interaction, it is known through mutagenesis studies that recognition is mediated by an 'arginine patch' formed by Arg38, Arg65, and Arg93[5, 24] (Figure 1) that binds to the PPant phosphate. The pocket with the arginine patch further contains Asp109 and Thr113 (Figure 1c).[5, 8]

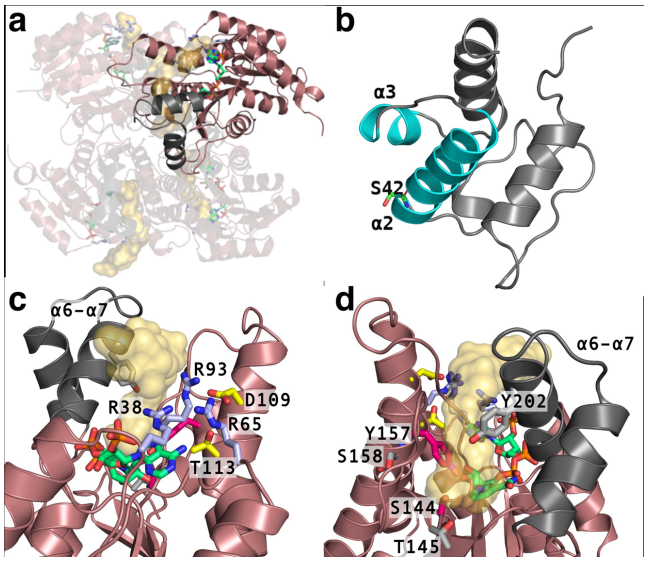

Figure 1. Features of *act*KR (PDB 2RH4)[8] and *act*ACP (PDB 2MVU)[25] related to *act*KR-*act*ACP-substrate complex formation. (a) The *act*KR tetramer, with NADPH's C atoms in green, arginine patch (R38, R65, R93) in light blue and binding sites for the substrate as transparent orange surfaces highlighted in each monomer. (b) *act*ACP with the α2 and α3 helices in cyan and the PPant-bearing Ser42 highlighted. (c) *act*KR monomer (chain D) viewed from the side of the arginine patch, with D109 and T113 shown (C atoms in yellow). α6-α7 helices and loop are shown in dark gray. (d) As (c) with 180° rotation highlighting putative catalytic residues for cyclization (**1** to **2**; T145, S158, and Y202; C atoms in light gray) and ketoreduction (**2** to **3**; S144, and Y157; C atoms in magenta).

The first transformation that likely takes place in *act*KR is the cyclization of *act*ACP-**1** (once spontaneously enolized) to yield *act*ACP-**2** (Scheme 1).[5] The combination of *act*ACP-**1** binding to *act*KR monomers via the arginine patch[6, 8] and octaketide **1** docking inside the *act*KR's long but narrow active site[5-6] probably allows the enzyme to exert strong regiocontrol that favours a C7 and C12 ring closure. C7-C12 cyclization is evident in the final product actinorhodin and the shunt product mutactin formed by the action of only the minimal PKS and *act*KR (Chart 1). In the absence of the *act*KR, C10-C15 cyclisation of **1** competes with the natural C7-C12 ring closure.[5-6] Structure-activity relationships and sequence conservation led to Thr145 and Ser158 being proposed to play a role in this stereocontrol.[5] Thr145 has been suggested to play a role in stabilizing the $O11^-$ enolate while Ser158 may assist in the proton transfer to O7 from the solvent.

The main (second) transformation in *act*KR—its ketoreduction of *act*ACP-**2**—is both regio- and stereoselective,[5] producing an alcohol group on C9 (Scheme 1). The first and rate-determining[26] step in this reaction involves hydride transfer from the *act*KR-bound NADPH to C9[7, 27] and (asynchronous concerted) proton abstraction by O9 from *act*KR:Tyr157. Stabilization is provided throughout the reaction by a hydrogen bond between O9 and *act*KR:Ser144 (Scheme 1). The chirality set by *act*KR at C9 remains unresolved; both **2** and **3** are too labile to be isolated. **3** is shuttled as *act*ACP-**3** to actinorhodin aromatase (*act*ARO) and aromatized to *act*ACP-**4**, leading to a loss of the stereochemical information. In the absence of *act*ARO, mutactin is generated, but its chirality has not been unambiguously confirmed; its designation as '*9S*' in Chart 1 is based on previous supposition.[6]

It has therefore not yet been possible to infer which stereoisomer and conformer of *act*ACP-**2**, if any, is preferentially formed and reduced within *act*KR; nor how. Therefore, to fully understand the factors that connect the regio- and stereoselectivity, both the protein-protein and protein-substrate interactions between *act*KR and *act*ACP-**1** should be considered in detail. Although binding models have been suggested,[5, 7, 24] no crystal structure of the complex exists and detail on the interactions between *act*ACP and *act*KR is lacking. Most solved enzyme-ACP complexes[28-40] feature FASs,[28-34] and only two feature a PKS component (namely, ketosynthase).[35-36] Moreover, to study protein-substrate interactions, a complex with *act*ACP-**1** is required, but this is unfeasible. In this work, we combine protein-protein docking, molecular dynamics (MD) simulations, 2D protein-NMR spectroscopy and hybrid quantum mechanics / molecular mechanics (QM/MM) simulations to obtain detailed information on *act*KR – *act*ACP binding and *act*KR – octaketide interactions: our aim is to provide a unified picture of *act*KR structure and function and address the lack of fundamental knowledge on type II PKSs.[1, 17, 22]

Materials and Methods

Protein-protein Docking. Rigid docking calculations of *act*KR–NADPH and apo *act*ACP were performed using the Bristol University Docking Engine (*BUDE*),[41] with GPU acceleration. The structure for *act*KR–NADPH was obtained from previous simulations[27] starting from PDB ID 2RH4,[8] and the structure of *act*ACP was taken from model 13 of the NMR ensemble PDB ID 2MVU[25] (see details in Supporting Information). To maximize docking efficiency, the search space was restricted to areas of each protein's accessible surface interfaces and excluded areas too far away from the arginine patch. For docking, a "generation zero" of 4600 poses was randomly generated for each of the 43625 possible pairs of chosen *act*KR–NADPH and *act*ACP surface points. The 50 highest-scoring poses were evolved into 2500 "generation-one children" using a Monte Carlo algorithm, and the process (50 new parents, 2500 new children) repeated to generation five, resulting in ~43000 fifth-generation binding modes. 17 binding modes (labeled **M4-M20**) were selected (based on *BUDE* score and the distance of *act*ACP:Ser42 to the arginine patch) and for comparison, three *act*KR–*act*ACP models obtained or derived from previous works[5, 24, 31] (**M1-M3**) were included. Detailed procedures and coordinates for all models are provided as Supporting Information.

MD simulations of actKR-actACP complexes. Tetrameric (*act*KR–NADPH)$_4$–(*act*ACP)$_4$ structures for molecular mechanical (MM) MD simulations were assembled from the docking results, initially using different docking models (**M1-M20**) at each *act*KR chain in the tetramer, without the PPant-octaketide (see Figure 2, series I_A). For three docking models that gave the most promising results in series I_A (**M10**, **M14** and **M17**), further simulations were run with four *act*ACPs from the same model bound to one *act*KR tetramer (see Figure 2, series I_B). For the model selected after NMR assessment (**M14**), further MD simulations of the tetrameric complex were performed after introducing the PPant-octaketide moiety (**2**), with all combinations of the possible cyclization conformers (stage II, Figure 2; Scheme 2; Table S3). **2** was modelled from different starting positions in the active sites of each system by finding a balance between: 1) conformational agreement with the PPant of octaketide mimics crystallized with KRs;[42-44] and 2) maintaining catalytic interactions with residues Ser144 and Tyr157. The latter was not possible with C9 positioned for pro-*R* hydride attack; starting structures therefore had *S* prochirality in all cases.[6] Compared to the MD simulations without PPant-octaketide, the α6-α7 loops of actKR and adjacent residues (188-229) were positioned in a more 'closed' form, with the Tyr202 side chain projecting inside the active site (and a water molecule bridging Tyr202 and the octaketide).[44]

For both stage I and II MD, all residues were in their standard protonation states (consistent with pK_a predictions from PROPKA 3.1)[45] with *act*KR His162 protonated on Nδ1 and His153 and His201 on Nε2 (according to the surrounding H-bond network). All systems were solvated in a rectangular box extending at least 11 Å from any protein atom and neutralized by addition of Na^+ ions. The *ff14SB* force field[46] and the TIP3P model[47] were used, alongside NADPH parameters from Holmberg and coworkers[48]. GAFF[49] parameters with HF/6-31(d) RESP point charges were used for the PPant-Ser42 fragment (details and libraries in SI; calculations in ioChem-BD).[50-51] Multiple independent 32 ns periodic-boundary MD runs were performed in the *NpT* ensemble (after an equilibration procedure), using a 2 fs timestep (with SHAKE for bonds containing hydrogen). The temperature was maintained at 303 K, in line with kinetic assays[8] and recommended assessment of protein-protein docking stability,[52] and pressure at 1 atm. All simulations are conducted using AMBER 16[53-54] with GPU acceleration where applicable. CPPTRAJ[55] is used for trajectory analysis and postprocessing. Further details on generation of starting structures and MD procedures are provided in Supporting Information.

QM/MM reaction simulation of ketoreduction. QM/MM MD Umbrella Sampling (US) reaction simulations were run with *sander* from AMBER 16.[56-57] Simulation conditions were identical to the MM MD production runs, except for a shorter time-step (1 vs. 2 fs) and no *SHAKE* restraints[58] on the QM region. This region was limited to one active site, and comprised the cyclooctaketide moiety of **2** from C4 to C16; Ser144 and Tyr157 side chains from Cβ; the nicotinamide moiety of NADPH up to the first ribose (Figure S2). The QM region was treated with the semiempirical method PM6[59] as used and benchmarked in our previous study on *act*KR (PM6 overestimates the barrier, but the mechanism is correct).[27] QM/MM MD US simulations of reductive hydride transfer from NADPH to **2**'s C9 were run as previously[27], using the difference ($x - y$) as reaction coordinate, where y is the distance NADPH:H^{-}–**2**:C9 and x is the distance NADPH: H^{-}–NADPH:C$_{H-}$ (Figure S2). Simulations were started from 11 or 12 different 'reactive conformations' selected from stage II MD runs for each of the three isomers of **2** for which reactive conformations were regularly sampled (*vide infra*). The reaction coordinate was followed using US windows 0.1 Å apart until reaching 1.8 Å, and free energy profiles were obtained by combining all sampling (~1 ns per isomer) using the weighted histogram analysis method.[60-61] Further details are reported in the Supporting Information.

2D-NMR titration of actKR into actACP. *act*KR[5] and uniformly ^{15}N labelled *act*ACP[25] were expressed and purified as described previously. All NMR data was acquired with a Varian *INOVA* 600 MHz spectrometer at 25 °C. Titrations of *act*KR into ^{15}N-labelled holo-*act*ACP were monitored by ^{1}H-^{15}N HSQC-TROSY experiments. The molar ratios of KR:ACP at each titration point were 0.08, 0.47, 0.33, 0.67, 1.00, 1.34, 1.67 and 2.34 respectively. Stock solution of KR was 1.66 mM KR in 100 mM potassium phosphate pH 6.5, 10 mM EDTA and 1mM DTT. This was added to 500 µl of 0.5 mM ^{15}N-labelled ACP in the same buffer.

Results and Discussion

Approach for actKR-actACP model generation and validation. To obtain and validate a reliable, detailed structural model for *act*ACP–**2** binding to the tetrameric *act*KR, a stepwise computational procedure was followed (Figure 2), guided by NMR spectroscopy. The general approach is in line with recent recommendations[1, 62] and previous work on related systems.[63-64] First, protein-protein docking was used to explore potential *act*KR – *act*ACP binding modes. Selected modes were then refined[52] through extensive classical molecular dynamics simulations, in absence of the PPant-substrate (Figure 2; Stage I). Structural analysis based on chemical shift perturbations of *act*ACP obtained from 2D ^{1}H-^{15}N HSQC *act*KR titration data helped select the most likely binding mode. Then, all four stereoisomers of **2** were modelled into this binding mode, using all 8 possible cyclized species, referred to as 'isomer-conformers' (see Scheme 2 below). Thereafter, detailed molecular mechanical and hybrid QM/MM molecular dynamics simulations test the enzyme-substrate interactions and expected reactivity (final two stages in Figure 2). In the following subsections, we describe results from each stage in more detail and discuss how the validated model informs on the origins of stereo- and regio-selectivity of *act*KR-*act*ACP.

ActKR-actACP Binding Poses from Docking and MD simulation. Previous work[5, 8] has indicated that the *act*ACP – *act*KR interaction is guided by a patch of three arginines on *act*KR (Figure 1), which recognize and bind the PPant phosphate attached to Ser42 in *act*ACP-**1**.[5, 24] Extensive protein-protein docking of an *act*KR monomer (with NADPH bound) and *act*ACP (in the absence of substrate) was assessed (*Protein-protein Docking* in Figure 2) alongside two previously suggested binding modes (**M1**[24] and **M2**),[5] and one (**M3**) derived from the crystal structure of *Escherichia coli* enoyl reductase FabI complexed to its ACP (PDB 2FHS).[31] By considering a combination of the interaction energy (BUDE docking score) and a cutoff for the distance (*d*(PPant–*act*KR)) between *act*ACP:Ser42:Cβ (bound to the Oγ which carries the PPant) and *act*KR:Arg38:Cζ (representing the arginine patch), henceforth referred to as Ser42-patch distance, we selected 17 further docking models (**M4**-**M20**) that are structurally distinct (see Supporting Information).

The full set of models **M1**–**M20** were then further assessed using classical molecular dynamics (MD; *MD Stage I* in Figure 2) simulations to compensate for the rigidity in docking and to help eliminate false positives.[52] For each model, 8 MD-refined binding poses were obtained through 8 independent MD simulations of 32 ns and subsequent clustering (series $\mathbf{I_A}$ in Figure 2, details in Supporting Information). For each MD refined binding pose (8 for each of the 20 docking models, i.e., 160 in total), interaction energy (*BUDE* score) and *d*(PPant–*act*KR) were measured (Figure S4). Binding modes **M1-M3**, **M5-8**, **M11**, **M12** and **M19** were deemed non-viable after MD refinement: all poses from **M2** and **M3** had large Ser42-patch distances (>24 Å) and unfavorable interaction energies (>–90 kJ mol^{-1}); all poses from **M1**,**M5-8** had Ser42-patch distances >9 Å (even though 24 poses out of 40 had interaction energies between –174 and –90 kJ mol^{-1}); all poses from **M11**, **M12** and **M19** had consistently poor interaction energies (>–90 kJ mol^{-1}).

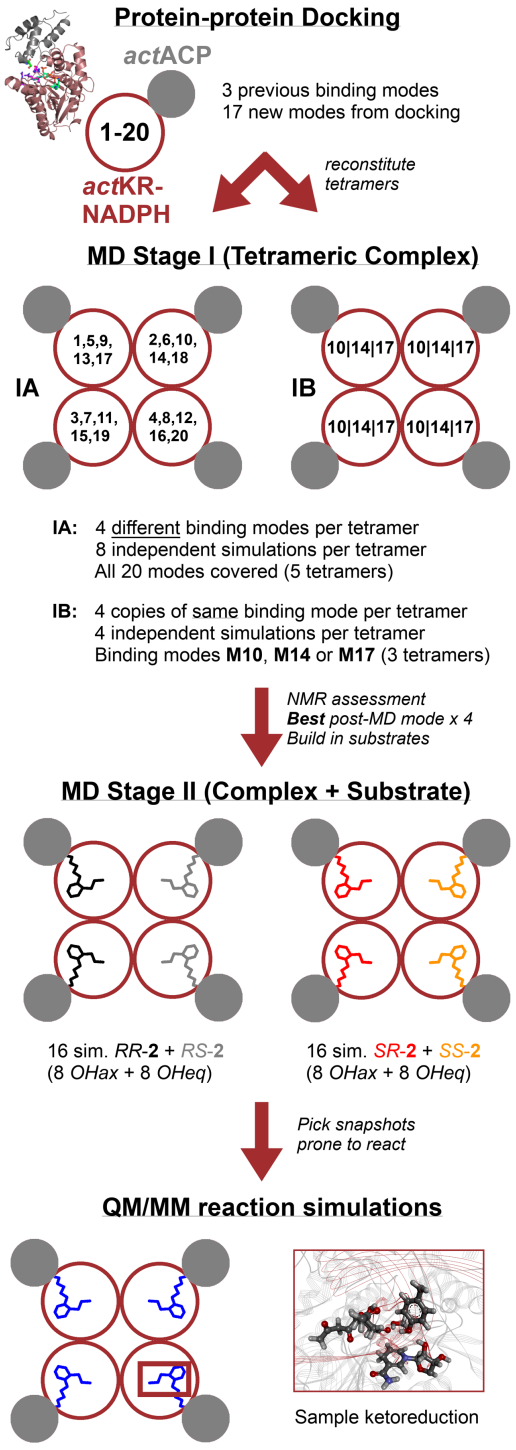

Figure 2. Overview of the computational procedure for *act*ACP-*act*KR model generation and validation. Protein-protein docking is followed by MD simulations in the absence of **2**. After assessment using *act*ACP-*act*KR NMR titration data, MD simulations in the presence of **2** and hybrid QM/MM reaction simulations are performed.

MD refinement of the remaining docking models (**M4**, **M9**, **M10**, **M13**–**M18** and **M20**) yielded several examples with good protein-protein interaction and compatibility with PPant insertion (low *BUDE* score and Ser42-patch distance,

d(PPant–*act*KR)). When applying thresholds of interaction energy below –90 kJ mol^{-1} and Ser42-patch distance below 9 Å (pink rectangle in Figure 3), there was one favorable binding pose each originating from docking models **M4**, **M9**, **M15**, **M16**, and **M20** (Figure S4); two originating from **M13** (Figure S4); three from **M18** (Figure S4); and as many as four from **M10** and **M14** and five from **M17** (Figure S4; triangles in Figure 3). All but two of these 23 refined poses improved their interaction energy from docking, indicating that the flexibility introduced by MD simulation generally improved the *act*KR-*act*ACP binding interface.

Based on the positive initial assessment (4 or 5 representative snapshots within the thresholds), docking models **M10**, **M14** and **M17** were selected for further MD simulation (Series $\mathbf{I_B}$; note that the next-best model **M18** is structurally similar to **M14**, with a RMSD between *act*ACP:Cα atoms of only 1.59 Å, and was therefore not selected). MD simulations were then performed using only one binding mode at each *act*KR–*act*ACP interface (using 4 × 32 ns simulations for each tetramer, Figure 2). Clustering then gave 16 additional representative snapshots for each binding mode. Using the same thresholds as before (*BUDE* score < –90 kJ mol^{-1}; *d*(PPant–*act*KR) < 9 Å), 13 additional binding poses were found for **M10**; 9 for **M14**, and just two for **M17** (Figure 3, Figure S5). (All but one of the additional poses improved their interaction energy from docking.) To further assist in the selection of the most promising binding poses, we also considered whether the Ser42-patch distance remained within 15% of its original value during the last 4 ns of the MD simulation from which each pose was selected (Figure 3; filled-in symbols). Combining this criterion with the best interaction energy (first) and the shortest Ser42-patch distance (second) resulted in the selection of refined poses $\mathbf{M10_{14IB}}$, $\mathbf{M14_{16IB}}$, and $\mathbf{M17_{1IA}}$ (see framed symbols in Figure 3 and structures in Figure 4). The subscripts denote the MD replica (number 14, 16, or 1) and series (IA or IB).

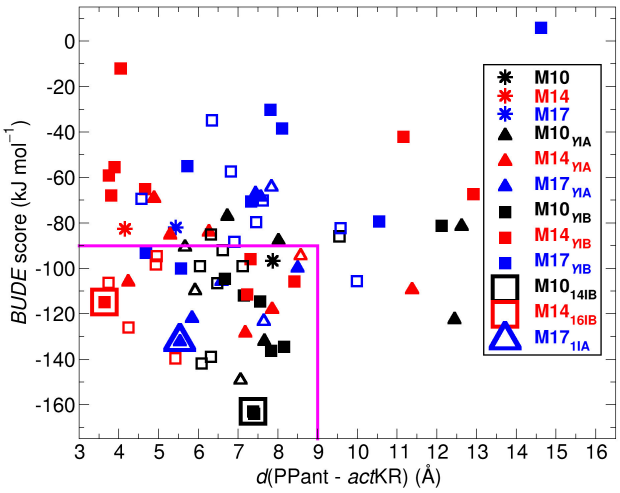

Figure 3. Refinement and ranking of docking models by MD simulation. *Act*KR–*act*ACP binding modes originating from MD simulations of M10 (black); M14 (red); and M17 (blue) are shown with their interaction energy (BUDE score, *y*-axis) and Ser42-patch distance (*d*(PPant–*act*KR), *x*-axis). Asterisks denote original docking modes; squares, those originating from series IA ($\mathbf{MX_{Y1A}}$; *X*=10,14,17; *Y* = 1-8); triangles, those originating from IB ($\mathbf{MX_{Y1B}}$; *Y* = 1-16). The area bound by magenta lines indicates the region with BUDE score < –90 kJ mol^{-1} and d(PPant–actKR) < 9 Å thresholds. Open triangles and squares refer to binding modes whose Ser42-patch distance deviates by more than 15% from its average value in the last 4 ns of the MD simulations from which they originate. The three binding modes selected for structural analysis and validation with NMR are highlighted by framed symbols.

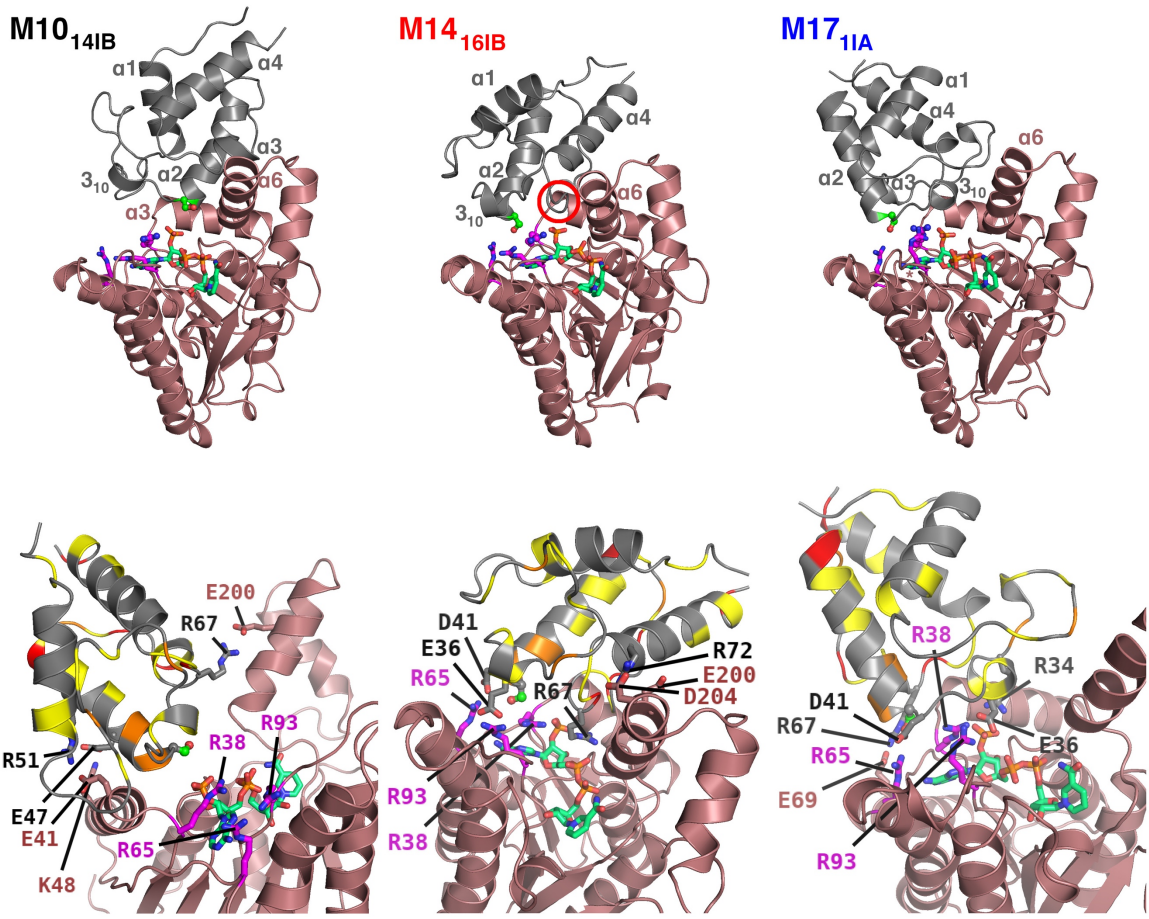

Figure 4. Putative *act*ACP–*act*KR binding modes **M10$_{14IB}$**, **M14$_{16IB}$**, and **M17$_{1IA}$** selected from docking and MD simulations. *Top 3 panels*: overview of *act*ACP–*act*KR binding modes, with *act*KR (off-red cartoon) in the same orientation; *act*ACP as gray cartoon. In **M14$_{16IB}$**, *act*ACP's 'gatekeeper' α3 helix is marked by a red circle; it is central to the *act*ACP-*act*KR interface and has lost some of its structure. NADPH, *act*ACP:Ser42, and the *act*KR arginine patch are shown (according to key below). *Bottom 3 panels*: magnification of the *act*ACP–*act*KR interfaces with the ACP backbone colored according to the magnitude of the measured chemical shift perturbations upon addition of *act*KR: $0.02 < \Delta\delta_{AV} < 0.04$ ppm in yellow, $0.04 < \Delta\delta_{AV} < 0.06$ ppm in orange and $\Delta\delta_{AV} \geqslant 0.06$ ppm in red (see Figure S6 for details). NADPH, *act*ACP:Ser42, the *act*KR arginine patch and *act*KR and *act*ACP residues implicated in salt bridges (Table S5) are labelled and rendered as sticks. *Key for all panels*: NADPH with C atoms in green; Arginine patch with C atoms in magenta; *act*ACP:Ser42 in ball-and-stick with bright green C atoms; H atoms omitted for clarity.

***Structural Analysis and 2D-NMR Validation of* act*ACP-*act*KR Binding Modes.** All three *act*KR–*act*ACP binding modes selected after docking and MD simulation (Figure 4) feature *act*ACP:Ser42 (at the *N*-terminus of *act*ACP's α2 helix) relatively close to Arg38. Only in **M14$_{16IB}$** and **M17$_{1IA}$**, however, are all three arginines in the patch[5, 8] positioned to capture the phosphate in the PPant moiety of **2** (Figure 4): *act*ACP:Ser42:Oγ is 3.4 and 5.2 Å away from center of mass of the arginine guanidinium moieties, respectively (vs. 12.9 Å away in **M10$_{14IB}$**). The occluded surface area is larger in **M14$_{16IB}$** (1747 Å^2) than in **M17$_{1IA}$** (1402 Å^2) and **M10$_{14IB}$** (1148 Å^2), indicating a better fit between *act*ACP and *act*KR in the former. All three binding modes exhibit several stable salt bridge interactions between *act*ACP and *act*KR (Table S5). In **M10$_{14IB}$**, however, no salt bridges are formed with the arginine patch[5, 24] or NADPH (with most contacts between the *act*ACP α2 and *act*KR α6 helices). In contrast, in **M14$_{16IB}$** and **M17$_{1IA}$** salt bridges are formed with the arginine patch by both *act*ACP:Asp41 and *act*ACP:Glu36, and with the phosphate moieties of NADPH by Arg67 (**M14$_{16IB}$**) or Arg34 (**M17$_{1IA}$**). In **M14$_{16IB}$**, actACP α3 is in the center of the *act*ACP–*act*KR interface, whereas the overall binding interaction in **M17$_{1IA}$** is dominated by the α1-α2 loop and does not involve α3.

To better distinguish the binding modes, we conducted ^{1}H-^{15}N HSQC titration experiments using ^{15}N labeled *act*ACP and unlabelled *act*KR (Supporting Information; Figure S6). Titration to an excess of *act*KR:*act*ACP showed distinct chemical shift perturbations (CSPs) particularly across the α2-α3 loop and α3. The largest magnitude CSPs are observed in this region (I60, D62, V68) and may also report on conformational changes in α3 as reported previously,[20] again pointing to the involvement of α3 in the *act*ACP–*act*KR interaction, as observed in **M14$_{16IB}$**. Further, residues of the flexible α1-α2 loop from T21-D29 exhibited exchange broadening; this loop is fully solvent-exposed only in **M14$_{16IB}$**.

In summary, structural analysis and NMR titration suggests that binding mode **M14$_{16IB}$** is most representative of the

*act*ACP–*act*KR complex, with the following features: (1) the *act*ACP 'gatekeeper' helix (α3) is central to the interface, occupying a cleft above the central NADPH phosphates; (2) the α4 helix interacts with the (mobile) α6 helix of *act*KR; (3) part of the α2-α3 loop, indicated by Hadfield et al. as being important for protein-protein interactions,[24] is also in contact with *act*KR; and (4) the α1-α2 loop is solvent exposed.

***Reactivity of ACP-bound Cyclized Octaketides in* actKR.** To assess the possible binding interactions of cyclized octaketides in *act*KR, we performed multiple independent MD simulations of *act*KR – *act*ACP with all possible cyclized conformers of **2** (MD stage II in Figure 2): C7-C12 cyclization of **1** can, in principle, lead to four different stereoisomers of **2** (color-coded in Scheme 2): *(7R,12R)*-**2** (henceforth *RR*-**2**; black); *(7R,12S)*-**2** (*RS*-**2**; gray); *(7S,12R)*-**2** (*SR*-**2**; red); and *(7S,12S)*-**2** (*SS*-**2**; orange). In turn, each of these four isomers can access two low-energy chair conformers (Scheme 2), with the C7 –OH substituent oriented either axially (**2**$_{OHax}$) or equatorially (**2**$_{OHeq}$). *act*ACP binding mode **M14$_{16IB}$** was used and the *act*KR α6–α7 loop was remodeled prior to MD simulation, based on an *act*KR-octaketide mimic complex structure,[44] in line with the suggested role of this loop in substrate recognition.[5] By using previous structural information[42-44] and satisfying contacts between **2** and catalytic residues, initial placements for the PPant and the octaketide moieties were generated (two alternative starting positions were used in order to explore a greater portion of conformational space; modelling details and coordinates are included as Supporting Information).

In the resulting MD simulations, the frequency of reactive poses (%$_{reac}$, defined by satisfying key distances; see Supporting Information)[65] of **2** towards C9 ketoreduction was monitored, and the combined %$_{reac}$ values (from 4 active sites × 8 replicas × 32 ns × four initial systems, see Table S3) were compared for each of the eight possible cyclization isomer-conformers of **2** (Figure 5, Table S6). *SR*-**2**$_{OHax}$ had the highest frequency of reactive poses (at 9.1%), followed by *RR*-**2**$_{OHeq}$ and *RS*-**2**$_{OHeq}$ (with 2.9% and 2.2%, respectively). The remaining five isomer-conformers had less than 2% reactive poses. Essentially all reactive poses are *pro-S*; only 12 *pro-R* poses were observed for all isomer-conformers (all for *SS*-**2**$_{OHeq}$) out of a total of >1.5 million snapshots. Our simulations thus show that **2** is (much) more prone to *pro-S* hydride attack at C9, in agreement with previous *in silico* models of the presentation of the polyketide substrate to NADPH[6] (see further below).

We further considered the relative free energies of all eight isomer-conformers (Figure 5, *y*-axis; QM calculation details in Supporting Information, optimized structures in ioChem-BD).[50-51] There is some degree of correlation between thermodynamic stability and the propensity to form reactive poses (e.g., Figure 6b) in the *act*KR active site: *SR*-**2**$_{OHax}$ is most stable, followed by *RS*-**2**$_{OHeq}$ and *RR*-**2**$_{OHeq}$ (0.9 kcal mol^{-1} and 1.4 kcal mol^{-1} higher in energy, respectively). The remaining isomers are significantly higher in energy (2.5 to 5.6 kcal mol^{-1}). There is also correlation between the frequency of reactive poses and stability of axial vs. equatorial C7-OH arrangement (especially for 12*R* isomers): in *7S* isomers, axial conformers are more stable and attain more reactive poses; in 7*R* isomers, the opposite is true.

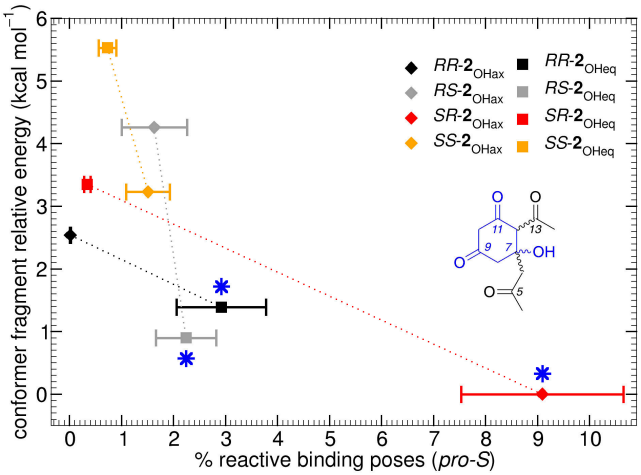

Figure 5. Comparison of QM energies and in-enzyme reactive poses of the different isomer-conformers of the cyclized octaketide **2**. *x*-axis: percentage of *pro-S* reactive binding poses (%$_{reac}$) present in stage II MD simulations (see Supporting Information for definition). *y*-axis: relative free energies of the C4-C14 fragment (SCS-MP2/6-31+G(*d,p*)//B3LYP/6-31+G(*d,p*), see Supporting Information for details) of the hydrogen-capped cyclopentaketide fragments (see inset). Lines are shown to guide the eye. (*) marks isomer-conformers chosen for QM/MM reaction simulations. Species are color-coded and labelled as in Scheme 2. Error bars along the *x*-axis are based on a leave-one-out procedure (see Supporting Information).

Scheme 2. C7-C12 Cyclization of the Natural Substrate of actKR with its Possible Stereoisomers and Chair Conformers.[a]

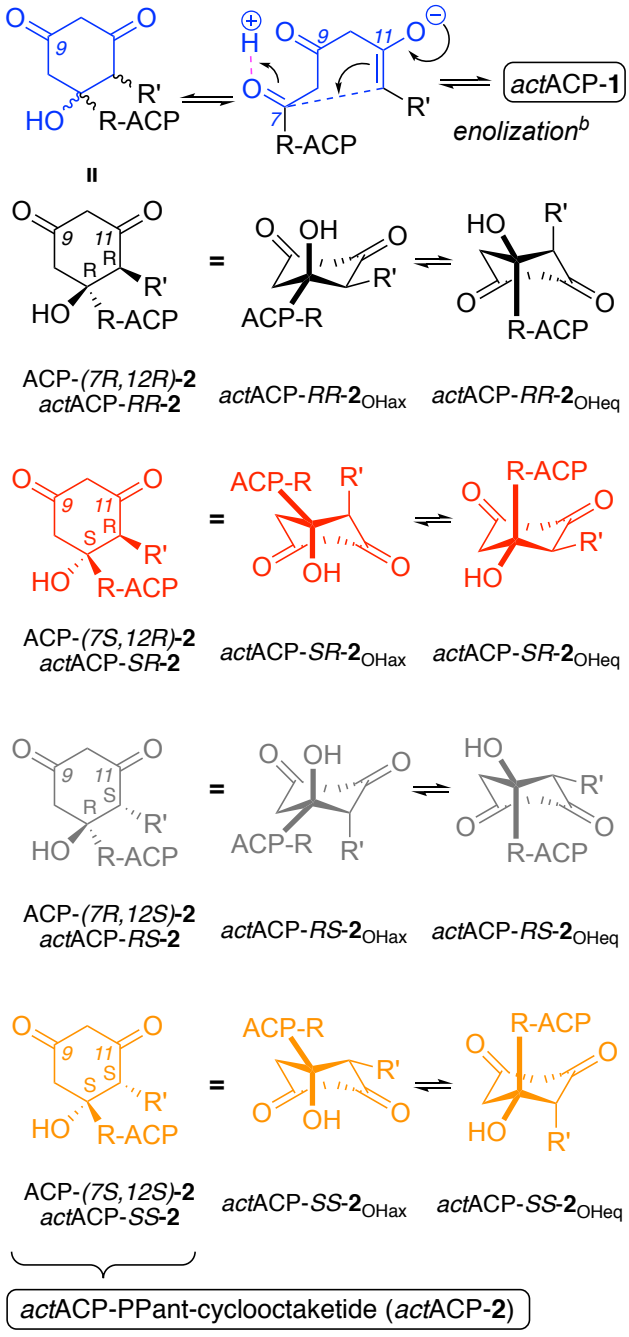

[a]Atoms in blue denote the portion of PPant-octaketide (**1**) forming the six-membered ring in the cyclized intermediate (**2**). [b] Loss of a proton on C12.

To simulate the chemical reaction itself, we selected three isomer-conformers of **2** (*SR*-**2**$_{OHax}$, *RS*-**2**$_{OHeq}$, and *RR*-**2**$_{OHeq}$). As indicated by the relatively infrequent occurrence of reactive poses (at most 9.1 % for *SR*-**2**$_{OHax}$), the cyclized octaketide spends the majority of the time 'in standby', i.e., bound in the active site with C9 close to the catalytic residues, but not quite ready for reaction (Figure 6a). Moving to a reactive conformation (e.g, Figure 6b) will thus come at a slight free energy cost (1.4, 2.1 or 2.3 kcal mol^{-1} at room temperature for *SR*-**2**$_{OHax}$, *RS*-**2**$_{OHeq}$, and *RR*-**2**$_{OHeq}$, respectively, based on ΔG=RT*ln*[% reactive poses]). For each, we performed combined quantum mechanical / molecular mechanical (QM/MM) MD simulations of ketoreduction at C9 (see *QM/MM reaction simulations* in Figure 2), using the same approach as our previous work on the reduction of *trans*-1-decalone by *act*KR.[27] The transition states and reaction barriers obtained here are similar (Figure 6, Figure S3), which demonstrates that the selected complexes modeled based on **M14$_{16IB}$** can indeed represent reactive *act*ACP-*act*KR poses, further validating this MD-refined model. As expected, the transition state corresponds to the hydride transfer between NADPH and C9, concerted with proton transfer from Tyr157 to O9 (Figure 6c). Subsequently, Tyr157 moves to coordinate to a NADP+ ribose hydroxyl (Figure 6d), ready for reprotonation through a proton shuttle likely involving the ribose and Lys161.[26-27] Notably, our simulations show energetically feasible reactions whilst the cyclized octaketide is bound to *act*ACP, confirming that the ACP-PPant tether does not need to be broken prior to ketoreduction by *act*KR (in contrast to what is expected for hedamycin KR).[9] The barriers to reaction are not significantly different between the three isomer-conformers, suggesting that *act*KR can facilitate ketoreduction to a similar extent in all three, via axial hydride attack at C9 (Scheme 1, Figure 6b-d). Whilst a preference for axial attack is in line with previous findings on the reduction of small alicyclic ketones by agents such as $[AlH_4]^-$ and $[BH_4]^-$,[66-67] it is in contrast with findings by Østergaard *et al.* on reduction of the small alicyclic *trans*-1-decalone by another ketoreductase,[68] and our own findings for its reduction by *act*KR itself.[27] It appears that the tendency of *act*KR to catalyze equatorial H^- attack in small, non-endogenous substrates can be overridden by factors such as binding site architecture, spatial constraints arising from *act*KR–*act*ACP binding, and the presence of oxygen substituents on C7 and C11.

Determinants of* actKR *Stereo- and Regioselectivity. The near-absence of *pro-R* reactive poses in our MD simulations (stage II) indicates that *S*-selectivity for ketoreduction at C9 in *act*KR is defined by its active site structure in combination with the position of the incoming PPant chain, as suggested previously[5-6] (Figure 1d; Figure 6; Figure S2). The side chains of the adjacent residues *act*KR:Thr145 (possibly stabilizing O11 during cyclization of **1** to **2**; Scheme 2)[5] and *act*KR:Ser144 (stabilizing O9 during ketoreduction; Scheme 1) form a relatively rigid template close to the nicotinamide ring of NADPH. When O11 and O9 bind to these residues upon arrival of **1** into the active site, C7-C12 cyclization to any isomer-conformer of **2** creates spatial constraints that strongly favor reductive hydride attack in a *pro-S* pose (i.e., 'from below' in Figure 6b-d).

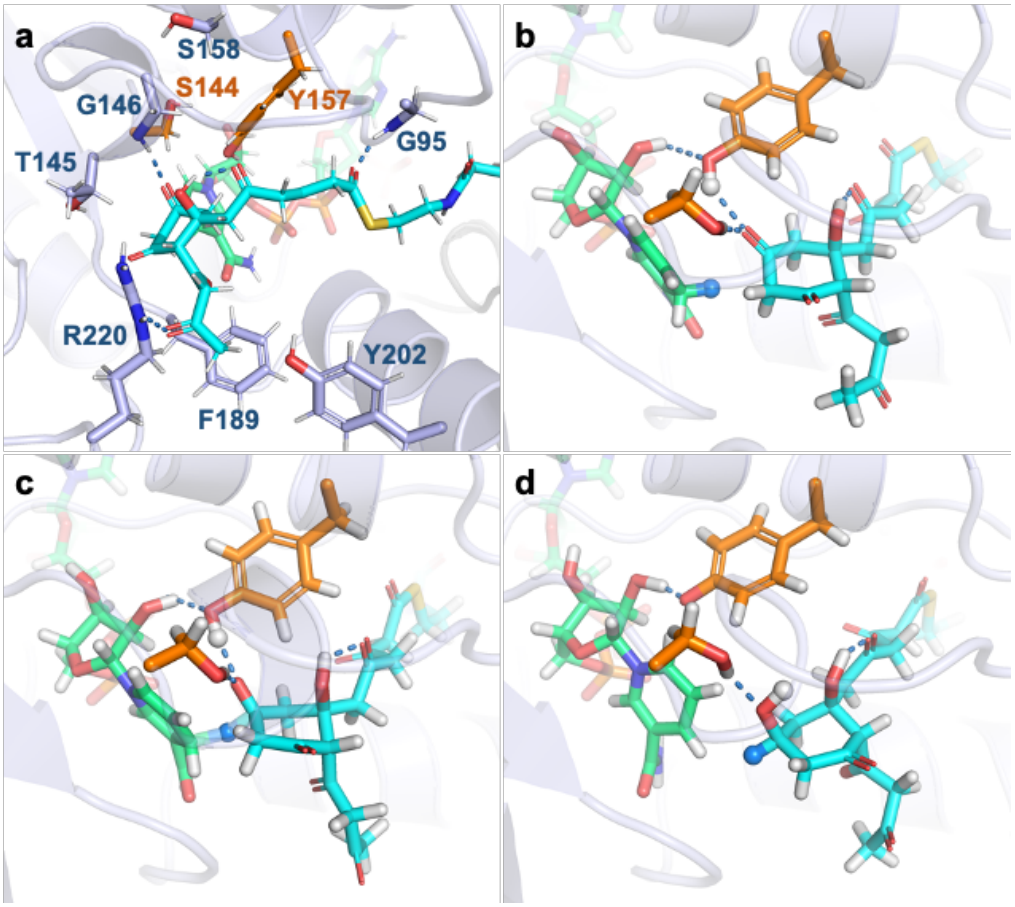

Figure 6. Key steps in the ketoreduction of *act*ACP-*SR*-**2**$_{OHax}$ by *act*KR. The sequence depicts the *pro-S* hydride attack on isomer-conformer *SR*-**2**$_{OHax}$. (a) Representative nonreactive snapshot of *act*ACP-*SR*-**2**$_{OHax}$ (C atoms in cyan) inside the active site of *act*KR, highlighting residues (sticks; C atoms light blue) that could be important for regioselectivity per our hydrogen bond analysis (see text). Catalytic residues Ser144, Tyr157 (C atoms in orange) and the NADPH cofactor (C atoms in green) are shown. Gly95:NH, part of the XGG motif,[5-6, 8] interacts frequently with **2**:O1; other residues are discussed in the text. (b) Reactive pose of *act*ACP-*SR*-**2**$_{OHax}$ poised for hydride transfer from NADPH. Hydride shown as blue sphere and *act*KR:Tyr157:Hη (i.e., –(O)H) as white sphere. (c) Transition state of the ketoreduction reaction, with hydride being transferred from NADPH to **2**:C9. (d) Product of ketoreduction, with Tyr157's phenolic proton transferred to **2**:O9.

The link between C7-C12 ring conformer stability and greater propensity for (*pro-S*) C9 ketoreduction (i.e., the most energetically stable isomer-conformers also give the highest number of reactive poses) merits further reflection as to why the *act*KR active site might have evolved to harness isomer-conformers *SR*-**2**$_{OHax}$, *RS*-**2**$_{OHeq}$ and *RR*-**2**$_{OHeq}$ in the first place. Perhaps the enzyme preferentially processes those conformers of **2** that are more likely to result after cyclization of **1**. In addition, *act*ARO—likely having evolved in tandem with *act*KR—might prefer the combination of *S* chirality at C9 alongside the three isomer-conformers to perform its conversion of **3** to **4** (although confirming this hypothesis would require detailed mechanistic studies of *act*ARO, which is beyond the scope of this work).

Apart from its stereoselectivity in ketoreduction, the other remarkable characteristic of *act*KR is its regioselectivity: namely, why cyclization occurs between C7 and C12 (if it occurs on *act*KR, rather than on *act*KS/CLF), and why ketoreduction then occurs specifically at C9 (with the link between the two already noted).[5] To investigate if and how the binding site architecture might drive regioselectivity, we examined the formation of hydrogen bonds (direct or water-mediated) between *act*KR and substrate oxygen atoms in MD trajectories from stage II (Figure 6a, full details in Tables S7 and S8). Hydrogen bonds between the cyclized octaketide moiety and *act*KR are rather transient during our simulations. Short-lived hydrogen bonds are consistent with **1** and **3** 'sliding' in and out of the binding channel, respectively, as suggested by Javidpour *et al*.,[5] as well as the 'in standby' conformation of the cyclized octaketide (with catalytically competent poses only being attained for a fraction of the simulation time, Figure 5). Hydrogen bonds directly relevant for ketoreduction at C9 are observed between O9 and Ser144 and Tyr157 on *act*KR (Scheme 1), but not as the most frequent (average frequencies, respectively, of 5.3 and 4.8% for *SR*-**2**, 4.3 and 4.3% for *RR*-**2**, and 3.0 and 1.8% for *RS*-**2**). Instead, the most frequent hydrogen bonding for O9 occurs with nearby backbone hydrogens of *act*KR:Phe189 (a residue whose importance was also noted experimentally)[5, 8] and *act*KR:Gly146 (Figure 6a, Table S7). Interactions with *act*KR:Ser144 and *act*KR:Tyr157's –OH hydrogens are typically mediated by water bridges when found

(Table S8). These interactions are consistent with isomers of **2** being held 'in standby' in the binding site (Figure 6a), with the C9=O9 carbonyl never far from reaching a reactive pose (Figure 6b). Only this carbonyl interacts with the key catalytic residues, thus achieving regioselectivity at C9.

The simulated isomers of **2** can be considered as the products of C7-C12 cyclization of **1** (Scheme 2), and their interactions may therefore reflect how such regioselective cyclization might be promoted by the *act*KR active site. One possible key interaction could be hydrogen bonding between O11 and *act*KR:Thr145's hydroxyl group; however, our simulations only indicate sporadic and indirect hydrogen bond interactions (through water bridges, Table S8). A different hydrogen bond interaction that may be relevant for cyclization, between **2**:O7/H7 and *act*KR:Tyr202's –OH group, is observed occasionally in simulations for most isomer-conformer pairs (Table S7, Table S8). This (highly conserved)[5] Tyr202 side chain, in its orientation towards the active site[44] (Figure 6a, Figure S2), could thus be involved in catalyzing regioselective C7-C12 cyclization, e.g. as proton donor to O7, or aiding proton transfer from the nearby His153 and His201. Other interactions that may be relevant for cyclization are the long-lived intramolecular hydrogen bond between **2**:H7 and **2**:O5, and the occasional water bridges between **2**:O5 and *act*KR:Tyr202's –OH, both of which may contribute to C7-C12 cyclization through stabilization of proton transfer to O7. Notably, interactions of **2**:O7/H7 with *act*KR:Ser158's hydroxyl group, previously proposed to play a role in proton donation in cyclization,[5] are hardly ever sampled. While these specific hydrogen bond interactions detected for O5, O7, and O11 may be structurally and/or electronically important factors for regioselective cyclization of **1** to **2**, further work is required to confirm the possible roles of *act*KR residues in C7-C12 cyclization, such as stabilization of the enolate species and the source for O7 protonation (e.g., involving Tyr202, His153 and/or His201).

Finally, we consider contacts at the extremities of the (cyclized) octaketide species. Zhao *et al.* recently used extensive MD simulations of *act*KR and a double mutant which affects chain-length specificity, together with octaketide and tetraketide substrate mimics.[44] They considered two previously proposed substrate entrance sites, a 'back-patch' near Q149/R220 and a 'front-patch', identical to the 'arginine patch'. In our work, only binding at the latter is considered, as this is enforced by the location of ACP, with the PPant phosphate group binding to the arginine patch. This is consistent with the preference of the PPant octaketide mimic found by Zhao *et al*.[44] For the octaketide, we find frequent and fairly persistent hydrogen bonds (direct or through bridging waters) between the start of the chain (O1) and the backbone *act*KR:Gly95:NH (Figure 6a). This glycine is part of the highly conserved XGG motif characterizing type II polyketide synthases, which has been suggested to be an anchor point for the PPant-octaketide to be presented to the *act*KR active site.[5-6] Our simulations further support this. At the other end, O15 forms frequent hydrogen bonds (direct or through bridging waters) with *act*KR:Arg220, located towards the *C*-terminus of the α7 loop and previously considered by mutagenesis[5] (Figure 6a). Arg220 can 'seal' the binding pocket at its far end (including through hydrogen bonding with *act*KR:Gln149,[8] forming the 'back-patch' that can support binding of short polyketides)[44] and could thus be a key factor for the regioselectivity of cyclization by helping the linear octaketide **1** buckle upon itself near O15, folding the C12-C16 fragment back onto C7-C11.

Conclusions

In the type II actinorhodin polyketide synthase, association between actinorhodin ketoreductase (*act*KR) and an actinorhodin acyl carrier protein (*act*ACP) carrying a phosphopantetheinylated octaketide results in the latter being inserted into the *act*KR active site (as **1** or cyclized as **2**). Subsequently **2** is stereoselectively reduced at C9=O9 to yield alicyclic chiral alcohol **3**. In this work, we have uncovered the most likely *act*ACP – *act*KR binding mode in atomic detail, using a combination of protein-protein docking, molecular dynamics simulations and NMR chemical shift perturbations. Then, further molecular dynamics simulations (including QM/MM reaction simulations) based on this binding mode are used investigate the mechanism and the sources of regio- and stereoselectivity of *act*KR towards its natural substrate.

After initial selection of simulation-refined docking models based on estimated binding affinity and proximity of *act*ACP:Ser42 to a 'patch' of three arginines on *act*KR (Arg38, Arg65, Arg93), one binding mode was found to be most consistent with our 2D NMR data and previous reports. In this mode, *act*ACP docks onto *act*KR with its α3 helix and the N-termini of α-helices 2 and 4. Subsequent simulations based on this binding mode of complexes with all possible C7-C12 cyclization isomers of **2** revealed an overwhelming preference for *pro-S* ketoreduction at C9=O9, particularly for the most thermodynamically stable cyclization isomer (i.e., *(7S,12R)*-**2** with C7-OH oriented axially). As well as establishing a link between chirality at C7/C12 and chirality at C9, this finding unequivocally confirms previous experimental data on mutactin inferring that C9 should be enantiopure;[6] it also strongly suggests that chirality at **3**:C9 should be *S* rather than *R*, and that *act*KR preferentially catalyzes axial hydride attack at C9. The binding mode of *act*ACP in conjunction with spatial features of the *act*KR active site are sufficient to cause the indicated *S*-selectivity.

QM/MM MD reaction simulations of C9 ketoreduction were performed for the three isomers of **2** that most frequently formed reaction competent binding poses. This indicated that *S*-selective ketoreduction is equally efficient for these isomers (i.e., no specific C7/C12 chirality is preferred in the chemical step) and our model yields energy barriers similar to those obtained with efficiently converted small molecules (further validating our proposed *act*ACP–*act*KR binding mode). Further analysis of our MD simulations of **2** inside *act*KR identified residues (such as Gly95 and Arg220) that are important for steering the binding of the substrate and holding it 'in standby' in the *act*KR active site, as well as those that may aid regioselective cyclization between C7 and C12.

In summary, we have combined protein-protein docking, extensive MD simulation, NMR and QM/MM reaction

simulations to produce and validate a detailed model of the *act*KR–*act*ACP interaction that is consistent with all currently available experimental data for cyclization and ketoreduction of the natural octaketide substrate.[5-6] The model obtained provides important mechanistic insights, demonstrating the use of multiscale atomistic simulations to improve our understanding of biocatalytic protein-protein complexes. We have shown that the specificity of the *act*KR–*act*ACP interaction, together with the architecture of the *act*KR active site, has direct implications for the elegant regio- and stereoselectivity of *act*KR towards its natural substrate. The information obtained can aid in future engineering of type II PKS ketoreductase/acyl carrier systems, e.g., to make them process alternative substrates; an important step towards building biocatalytic systems that can yield new polyketide derivatives.

ASSOCIATED CONTENT

Supporting Information. The Supporting Information is available free of charge on the ACS Publications website at DOI:.
Additional details on docking calculations, construction of starting structures, parametrization of isomer-conformers of **2**, MD simulation and analysis, NMR data, details of QM/MM simulations, analysis of hydrogen bonds in MD runs in **II**. (PDF)
Input files for protein-protein docking; structures of **M1-M20**, $\mathbf{M10}_{\mathbf{14IB}}$, $\mathbf{M14}_{\mathbf{16IB}}$ and $\mathbf{M17}_{\mathbf{11A}}$ in PDB format; *AMBER* input (topologies and coordinates) for all runs in $\mathbf{I}_{\mathbf{A}}$, $\mathbf{I}_{\mathbf{B}}$, and **II**; modified force field parameters for the PPant moiety and octaketide portions of **2**. (ZIP)

AUTHOR INFORMATION

Corresponding Author

* E-mail: Marc.VanderKamp@bristol.ac.uk

Present Addresses

^ Stefano A. Serapian: Department of Organic Chemistry, University of Pavia, viale Taramelli 10, 27100, Pavia, Italy.

Orcid

Stefano A. Serapian: 0000-0003-0122-8499
John Crosby: 0000-0002-8389-7102
Matthew P. Crump: 0000-0002-7868-5818
Marc W. van der Kamp: 0000-0002-8060-3359

Author Contributions

SAS and MWK designed the *in silico* experiments, SAS performed experiments, MWK devised the project. JC and MPC designed and performed the NMR experiments. SAS, MPC and MWK analyzed results and wrote the manuscript.

Funding Sources

MWK and SAS thank BBSRC for funding (David Phillips Fellowship to MWK, grant BB/M026280/1). MPC and JC also thank BBSRC for funding (grant BB/F014570/1).

ACKNOWLEDGMENT

This work was conducted using the computational facilities of the Advanced Computing Research Centre of the University of Bristol. The authors thank Prof. Shiou-Chan Tsai (Sheryl) and Gabriel O. Moreno (UC Irvine) for sharing their crystallographic data. SAS thanks Amaurys Ávila-Ibarra (University of Bristol) for his guidance with the protein-protein docking. JC and MPC thank Louise Pearson for her assistance with the NMR experiments.

REFERENCES

1. Chen, A.; Re, R. N.; Burkart, M. D., Type II Fatty Acid and Polyketide Synthases: Deciphering Protein–Protein and Protein–Substrate Interactions. *Nat. Prod. Rep.* **2018,** *35*, 1029-1045.
2. Hertweck, C.; Luzhetskyy, A.; Rebets, Y.; Bechthold, A., Type II Polyketide Synthases: Gaining a Deeper Insight into Enzymatic Teamwork. *Nat. Prod. Rep.* **2007,** *24*, 162-190.
3. Zhang, Z.; Pan, H. X.; Tang, G. L., New Insights into Bacterial Type II Polyketide Biosynthesis. *F1000Research* **2017,** *6*, 172.
4. Du, D.; Katsuyama, Y.; Shin‐ya, K.; Ohnishi, Y., Reconstitution of a Type II Polyketide Synthase That Catalyzes Polyene Formation. *Angew. Chem. Int. Ed.* **2018,** *57*, 1954-1957.
5. Javidpour, P.; Bruegger, J.; Srithahan, S.; Korman, Tyler P.; Crump, Matthew P.; Crosby, J.; Burkart, Michael D.; Tsai, S.-C., The Determinants of Activity and Specificity in Actinorhodin Type II Polyketide Ketoreductase. *Chem. Biol.* **2013,** *20*, 1225-1234.
6. Javidpour, P.; Korman, T. P.; Shakya, G.; Tsai, S.-C., Structural and Biochemical Analyses of Regio- and Stereospecificities Observed in a Type II Polyketide Ketoreductase. *Biochemistry* **2011,** *50*, 4638-4649.
7. Korman, T. P.; Hill, J. A.; Vu, T. N.; Tsai, S.-C., Structural Analysis of Actinorhodin Polyketide Ketoreductase: Cofactor Binding and Substrate Specificity. *Biochemistry* **2004,** *43*, 14529-14538.
8. Korman, T. P.; Tan, Y.-H.; Wong, J.; Luo, R.; Tsai, S.-C., Inhibition Kinetics and Emodin Cocrystal Structure of a Type II Polyketide Ketoreductase. *Biochemistry* **2008,** *47*, 1837-1847.
9. Javidpour, P.; Das, A.; Khosla, C.; Tsai, S.-C., Structural and Biochemical Studies of the Hedamycin Type II Polyketide Ketoreductase (HedKR): Molecular Basis of Stereo- and Regiospecificities. *Biochemistry* **2011,** *50*, 7426-7439.
10. Noey, E. L.; Tibrewal, N.; Jiménez-Osés, G.; Osuna, S.; Park, J.; Bond, C. M.; Cascio, D.; Liang, J.; Zhang, X.; Huisman, G. W.; Tang, Y.; Houk, K. N., Origins of Stereoselectivity in Evolved Ketoreductases. *Proc. Natl. Acad. Sci. U. S. A.* **2015,** *112*, E7065-E7072.
11. Tang, Y.; Lee, H. Y.; Tang, Y.; Kim, C.-Y.; Mathews, I.; Khosla, C., Structural and Functional Studies on SCO1815: A B-Ketoacyl-Acyl Carrier Protein Reductase from Streptomyces Coelicolor A3(2). *Biochemistry* **2006,** *45*, 14085-14093.
12. Valentic, T. R.; Jackson, D. R.; Brady, S. F.; Tsai, S.-C., Comprehensive Analysis of a Novel Ketoreductase for Pentangular Polyphenol Biosynthesis. *ACS Chem. Biol.* **2016,** *11*, 3421-3430.
13. Huisman, G. W.; Liang, J.; Krebber, A., Practical Chiral Alcohol Manufacture Using Ketoreductases. *Curr. Opin. Chem. Biol.* **2010,** *14*, 122-129.
14. Moore, J. C.; Pollard, D. J.; Kosjek, B.; Devine, P. N., Advances in the Enzymatic Reduction of Ketones. *Acc. Chem. Res.* **2007,** *40*, 1412-1419.
15. McDaniel, R.; Ebert-Khosla, S.; Hopwood, D. A.; Khosla, C., Rational Design of Aromatic Polyketide Natural Products by Recombinant Assembly of Enzymatic Subunits. *Nature* **1995,** *375*, 549.
16. Nivina, A.; Yuet, K. P.; Hsu, J.; Khosla, C., Evolution and Diversity of Assembly-Line Polyketide Synthases. *Chem. Rev.* **2019,** *119*, 12524-12547.
17. Neves, R. P. P.; Ferreira, P.; Medina, F. E.; Paiva, P.; Sousa, J. P. M.; Viegas, M. F.; Fernandes, P. A.; Ramos, M. J., Engineering of Pks Megaenzymes—a Promising Way to Biosynthesize High-Value Active Molecules. *Top. Catal.* **2021**.
18. Moretto, L.; Vance, S.; Heames, B.; Broadhurst, R. W., Dissecting How Modular Polyketide Synthase Ketoreductases Interact with Acyl Carrier Protein-Attached Substrates. *Chem. Commun.* **2017,** *53*, 11457-11460.
19. Yadav, U.; Arya, R.; Kundu, S.; Sundd, M., The "Recognition Helix" of the Type II Acyl Carrier Protein (ACP) Utilizes a "Ubiquitin Interacting Motif (Uim)"-Like Surface to Bind Its Partners. *Biochemistry* **2018,** *57*, 3690-3701.
20. Colizzi, F.; Masetti, M.; Recanatini, M.; Cavalli, A., Atomic-Level Characterization of the Chain-Flipping Mechanism in Fatty-Acids Biosynthesis. *J. Phys. Chem. Lett.* **2016,** *7*, 2899-904.
21. Schiebel, J.; Chang, A.; Merget, B.; Bommineni, G. R.; Yu, W.; Spagnuolo, L. A.; Baxter, M. V.; Tareilus, M.; Tonge, P. J.; Kisker, C.; Sotriffer, C. A., An Ordered Water Channel in Staphylococcus Aureus FabI: Unraveling the Mechanism of Substrate Recognition and Reduction. *Biochemistry* **2015,** *54*, 1943-55.
22. Sulpizio, A.; Crawford, C. E. W.; Koweek, R. S.; Charkoudian, L. K., Probing the Structure and Function of Acyl Carrier Proteins to

Unlock the Strategic Redesign of Type II Polyketide Biosynthetic Pathways. *J. Biol. Chem.* **2021,** *296*, 100328.
23. Maršavelski, A., A Novel Antimicrobial Target—Expanded and Revisited Mode of Action of Pantothenamides. *RSC Adv.* **2016,** *6*, 44888-44895.
24. Hadfield, A. T.; Limpkin, C.; Teartasin, W.; Simpson, T. J.; Crosby, J.; Crump, M. P., The Crystal Structure of the ActIII Actinorhodin Polyketide Reductase: Proposed Mechanism for ACP and Polyketide Binding. *Struct.* **2004,** *12*, 1865-1875.
25. Evans, S. E.; Williams, C.; Arthur, C. J.; Płoskoń, E.; Wattana-amorn, P.; Cox, R. J.; Crosby, J.; Willis, C. L.; Simpson, T. J.; Crump, M. P., Probing the Interactions of Early Polyketide Intermediates with the Actinorhodin ACP from S. Coelicolor A3(2). *J. Mol. Biol.* **2009,** *389*, 511-528.
26. Medina, F. E.; Neves, R. P. P.; Ramos, M. J.; Fernandes, P. A., A QM/MM Study of the Reaction Mechanism of Human B-Ketoacyl Reductase. *Phys. Chem. Chem. Phys.* **2017,** *19*, 347-355.
27. Serapian, S. A.; van der Kamp, M. W., Unpicking the Cause of Stereoselectivity in Actinorhodin Ketoreductase Variants with Atomistic Simulations. *ACS Catal.* **2019,** *9*, 2381-2394.
28. Dodge, G. J.; Patel, A.; Jaremko, K. L.; McCammon, J. A.; Smith, J. L.; Burkart, M. D., Structural and Dynamical Rationale for Fatty Acid Unsaturation in Escherichia Coli. *Proc. Natl. Acad. Sci. U. S. A.* **2019,** *116*, 6775-6783.
29. Milligan, J. C.; Lee, D. J.; Jackson, D. R.; Schaub, A. J.; Beld, J.; Barajas, J. F.; Hale, J. J.; Luo, R.; Burkart, M. D.; Tsai, S.-C., Molecular Basis for Interactions between an Acyl Carrier Protein and a Ketosynthase. *Nat. Chem. Biol.* **2019,** *15*, 669-671.
30. Nguyen, C.; Haushalter, R. W.; Lee, D. J.; Markwick, P. R. L.; Bruegger, J.; Caldara-Festin, G.; Finzel, K.; Jackson, D. R.; Ishikawa, F.; O'Dowd, B.; McCammon, J. A.; Opella, S. J.; Tsai, S.-C.; Burkart, M. D., Trapping the Dynamic Acyl Carrier Protein in Fatty Acid Biosynthesis. *Nature* **2014,** *505*, 427-431.
31. Rafi, S.; Novichenok, P.; Kolappan, S.; Stratton, C. F.; Rawat, R.; Kisker, C.; Simmerling, C.; Tonge, P. J., Structure of Acyl Carrier Protein Bound to FabI, the FASII Enoyl Reductase from Escherichia Coli. *J. Biol. Chem.* **2006,** *281*, 39285-39293.
32. Shen, S.; Hang, X.; Zhuang, J.; Zhang, L.; Bi, H.; Zhang, L., A Back-Door Phenylalanine Coordinates the Stepwise Hexameric Loading of Acyl Carrier Protein by the Fatty Acid Biosynthesis Enzyme B-Hydroxyacyl-Acyl Carrier Protein Dehydratase (Fabz). *Int. J. Biol. Macromol.* **2019,** *128*, 5-11.
33. Zhang, L.; Xiao, J.; Xu, J.; Fu, T.; Cao, Z.; Zhu, L.; Chen, H.-Z.; Shen, X.; Jiang, H.; Zhang, L., Crystal Structure of Fabz-ACP Complex Reveals a Dynamic Seesaw-Like Catalytic Mechanism of Dehydratase in Fatty Acid Biosynthesis. *Cell Research* **2016,** *26*, 1330-1344.
34. Masoudi, A.; Raetz, C. R. H.; Zhou, P.; Pemble Iv, C. W., Chasing Acyl Carrier Protein through a Catalytic Cycle of Lipid a Production. *Nature* **2014,** *505*, 422-426.
35. Herbst, D. A.; Huitt-Roehl, C. R.; Jakob, R. P.; Kravetz, J. M.; Storm, P. A.; Alley, J. R.; Townsend, C. A.; Maier, T., The Structural Organization of Substrate Loading in Iterative Polyketide Synthases. *Nat. Chem. Biol.* **2018,** *14*, 474-479.
36. Bräuer, A.; Zhou, Q.; Grammbitter, G. L. C.; Schmalhofer, M.; Rühl, M.; Kaila, V. R. I.; Bode, H. B.; Groll, M., Structural Snapshots of the Minimal Pks System Responsible for Octaketide Biosynthesis. *Nat. Chem.* **2020,** *12*, 755-763.
37. Fox, N. G.; Yu, X.; Feng, X.; Bailey, H. J.; Martelli, A.; Nabhan, J. F.; Strain-Damerell, C.; Bulawa, C.; Yue, W. W.; Han, S., Structure of the Human Frataxin-Bound Iron-Sulfur Cluster Assembly Complex Provides Insight into Its Activation Mechanism. *Nat. Commun.* **2019,** *10*, 2210.
38. Kreamer, N. N. K.; Chopra, R.; Caughlan, R. E.; Fabbro, D.; Fang, E.; Gee, P.; Hunt, I.; Li, M.; Leon, B. C.; Muller, L.; Vash, B.; Woods, A. L.; Stams, T.; Dean, C. R.; Uehara, T., Acylated-Acyl Carrier Protein Stabilizes the Pseudomonas Aeruginosa Waap Lipopolysaccharide Heptose Kinase. *Sci. Rep.* **2018,** *8*, 14124.
39. Agarwal, V.; Lin, S.; Lukk, T.; Nair, S. K.; Cronan, J. E., Structure of the Enzyme-Acyl Carrier Protein (ACP) Substrate Gatekeeper Complex Required for Biotin Synthesis. *Proc. Natl. Acad. Sci. U. S. A.* **2012,** *109*, 17406-17411.
40. Cryle, M. J.; Schlichting, I., Structural Insights from a P450 Carrier Protein Complex Reveal How Specificity Is Achieved in the $P450_{BioI}$ ACP Complex. *Proc. Natl. Acad. Sci. U. S. A.* **2008,** *105*, 15696-15701.
41. McIntosh-Smith, S.; Price, J.; Sessions, R. B.; Ibarra, A. A., High Performance in Silico Virtual Drug Screening on Many-Core Processors. *Int. J. High Perform. Comput. Appl.* **2015,** *29*, 119-134.
42. Ellis, B. D.; Milligan, J. C.; White, A. R.; Duong, V.; Altman, P. X.; Mohammed, L. Y.; Crump, M. P.; Crosby, J.; Luo, R.; Vanderwal, C. D.; Tsai, S.-C., An Oxetane-Based Polyketide Surrogate to Probe Substrate Binding in a Polyketide Synthase. *J. Am. Chem. Soc.* **2018,** *140*, 4961-4964.
43. Li, Y.; Fiers, W. D.; Bernard, S. M.; Smith, J. L.; Aldrich, C. C.; Fecik, R. A., Polyketide Intermediate Mimics as Probes for Revealing Cryptic Stereochemistry of Ketoreductase Domains. *ACS Chem. Biol.* **2014,** *9*, 2914-2922.
44. Zhao, S.; Ni, F.; Qiu, T.; Wolff, J. T.; Tsai, S. C.; Luo, R., Molecular Basis for Polyketide Ketoreductase-Substrate Interactions. *Int. J. Mol. Sci.* **2020,** *21*.
45. Søndergaard, C. R.; Olsson, M. H. M.; Rostkowski, M.; Jensen, J. H., Improved Treatment of Ligands and Coupling Effects in Empirical Calculation and Rationalization of pKa Values. *J. Chem. Theory Comput.* **2011,** *7*, 2284-2295.
46. Maier, J. A.; Martinez, C.; Kasavajhala, K.; Wickstrom, L.; Hauser, K. E.; Simmerling, C., ff14SB: Improving the Accuracy of Protein Side Chain and Backbone Parameters from ff99SB. *J. Chem. Theory Comput.* **2015,** *11*, 3696-3713.
47. Jorgensen, W. L.; Chandrasekhar, J.; Madura, J. D.; Impey, R. W.; Klein, M. L., Comparison of Simple Potential Functions for Simulating Liquid Water. *J. Chem. Phys.* **1983,** *79*, 926-935.
48. Holmberg, N.; Ryde, U.; Bulow, L., Redesign of the Coenzyme Specificity in L-Lactate Dehydrogenase from Bacillus Stearothermophilus Using Site-Directed Mutagenesis and Media Engineering. *Protein Eng.* **1999,** *12*, 851-856.
49. Wang, J.; Wolf, R. M.; Caldwell, J. W.; Kollman, P. A.; Case, D. A., Development and Testing of a General Amber Force Field. *J. Comput. Chem.* **2004,** *25*, 1157-1174.
50. A collection of relevant calculations is available on the io-ChemBD server. https://doi.org/10.19061/iochem-bd-6-101
51. Álvarez-Moreno, M.; de Graaf, C.; López, N.; Maseras, F.; Poblet, J. M.; Bo, C., Managing the Computational Chemistry Big Data Problem: The ioChem-BD Platform. *J. Chem. Inf. Model.* **2015,** *55*, 95-103.
52. Radom, F.; Plückthun, A.; Paci, E., Assessment of Ab Initio Models of Protein Complexes by Molecular Dynamics. *PLoS Comput. Biol.* **2018,** *14*, e1006182.
53. Case, D. A.; Cheatham, T. E.; Darden, T.; Gohlke, H.; Luo, R.; Merz, K. M.; Onufriev, A.; Simmerling, C.; Wang, B.; Woods, R. J., The Amber Biomolecular Simulation Programs. *J. Comput. Chem.* **2005,** *26*, 1668-1688.
54. Case, D. A.; Cerutti, D. S.; Cheatham, T. E.; Darden, T. A.; Duke, R. E.; Giese, T. J.; Gohlke, H.; Götz, A. W.; Greene, D.; Homeyer, N.; Izadi, S.; Kovalenko, A.; Lee, T. S.; Le Grand, S.; Li, P.; Lin, C.; Liu, J.; Luchko, T.; Luo, R.; Mermelstein, D.; Merz, K. M.; Monard, G.; Nguyen, H.; Omelyan, I.; Onufriev, A.; Pan, F.; Qi, R.; Roe, D. R.; Roitberg, A. E.; Sagui, C.; Simmerling, C. L.; Botello-Smith, W. M.; Swails, J. M.; Walker, R. C.; Wang, J.; Wolf, R. M.; Wu, X.; Xiao, L.; York, D. M.; Kollman, P. A. *Amber 2017*, University of California, San Francisco: 2017.
55. Roe, D. R.; Cheatham, T. E., PTRAJ and CPPTRAJ: Software for Processing and Analysis of Molecular Dynamics Trajectory Data. *J. Chem. Theory Comput.* **2013,** *9*, 3084-3095.
56. Seabra, G. d. M.; Walker, R. C.; Elstner, M.; Case, D. A.; Roitberg, A. E., Implementation of the SCC-DFTB Method for Hybrid QM/MM Simulations within the Amber Molecular Dynamics Package. *J. Phys. Chem. A* **2007,** *111*, 5655-5664.
57. Walker, R. C.; Crowley, M. F.; Case, D. A., The Implementation of a Fast and Accurate QM/MM Potential Method in Amber. *J. Comput. Chem.* **2008,** *29*, 1019-1031.
58. Shuichi, M.; Kollman, P. A., Settle: An Analytical Version of the Shake and Rattle Algorithm for Rigid Water Models. *J. Comput. Chem.* **1992,** *13*, 952-962.
59. Stewart, J. J. P., Optimization of Parameters for Semiempirical Methods V: Modification of NDDO Approximations and Application to 70 Elements. *J. Mol. Model.* **2007,** *13*, 1173-1213.
60. Kumar, S.; Rosenberg, J. M.; Bouzida, D.; Swendsen, R. H.; Kollman, P. A., The Weighted Histogram Analysis Method for Free-Energy Calculations on Biomolecules. I. The Method. *J. Comput. Chem.* **1992,** *13*, 1011-1021.

61. Kumar, S.; Rosenberg, J. M.; Bouzida, D.; Swendsen, R. H.; Kollman, P. A., Multidimensional Free-Energy Calculations Using the Weighted Histogram Analysis Method. *J. Comput. Chem.* **1995,** *16*, 1339-1350.
62. Rout, M. P.; Sali, A., Principles for Integrative Structural Biology Studies. *Cell* **2019,** *177*, 1384-1403.
63. Anand, S.; Mohanty, D., Modeling Holo-ACP:DH and Holo-ACP:KR Complexes of Modular Polyketide Synthases: A Docking and Molecular Dynamics Study. *BMC Struct. Biol.* **2012,** *12*, 10-20.
64. Viegas, M. F.; Neves, R. P. P.; Ramos, M. J.; Fernandes, P. A., Modeling of Human Fatty Acid Synthase and in Silico Docking of Acyl Carrier Protein Domain and Its Partner Catalytic Domains. *J. Phys. Chem. B* **2018,** *122*, 77-85.
65. By "reactive pose", we mean an enzyme-substrate complex positioned such that the substrate is in place for the chemical reaction to start; others have recently referred to this as a "near attack conformation" or NAC.
66. Di Maio, G.; Mascia, M. G.; Vecchi, E., Does Substituent's Conformation Influence the Kinetics of Reduction Reactions on Trans-4-X-Decal-1-Ones and to What Extent? *Tetrahedron* **2002,** *58*, 3313-3318.
67. Wu, Y. D.; Tucker, J. A.; Houk, K. N., Stereoselectivities of Nucleophilic Additions to Cyclohexanones Substituted by Polar Groups. Experimental Investigation of Reductions of Trans-Decalones and Theoretical Studies of Cyclohexanone Reductions. The Influence of Remote Electrostatic Effects. *J. Am. Chem. Soc.* **1991,** *113*, 5018-5027.
68. Østergaard, L. H.; Kellenberger, L.; Cortés, J.; Roddis, M. P.; Deacon, M.; Staunton, J.; Leadlay, P. F., Stereochemistry of Catalysis by the Ketoreductase Activity in the First Extension Module of the Erythromycin Polyketide Synthase. *Biochemistry* **2002,** *41*, 2719-2726.